SUPPLEMENTARY MATERIAL FOR

Constraining the Thermochemical Structure of Mars through Joint Inversion of Multidisciplinary Geophysical Data

Mélanie Drilleau[1], **Henri Samuel**[1], **Olivier Verhoeven**[2], **Attilio Rivoldini**[3], **Max Collinet**[4], **Raphaël F. Garcia**[5], **Philippe Lognonné**[1]

[1]Université Paris Cité, Institut de physique du globe de Paris, CNRS, Paris, France
[2]Nantes Université, Université d'Angers, Le Mans Université, CNRS, UMR 6112, Laboratoire de Planétologie et Géosciences, UAR 3281, Observatoire des Sciences de l'Univers de Nantes Atlantique, Nantes, France
[3]Royal Observatory of Belgium, Brussels, Belgium
[4]Institute of Life, Earth and Environment (ILEE), Namur University, Namur, Belgium
[5]Institut Supérieur de l'Aéronautique et de l'Espace ISAE-SUPAERO, Université de Toulouse, Toulouse, France

S. 1 Datafit of the inversion of individual data sets

Figures S1.1 and S1.2 show the data fit estimates of the inversion of the individual data sets, for the non-BML and BML sets, respectively.

S. 2 Individual inversion of electrical conductivity data: Output temperature and electrical conductivity profiles

Figures S2.1 and S2.2 show, in green, the output temperature and electrical conductivity profiles obtained from the inversion using electrical conductivity data only, for the non-BML and BML sets, respectively. The output models from the joint inversion are also indicated: in red (F1 models) and black (F2 models) for the non-BML set, and in black for the BML set. These profiles correspond to those shown in Figures 5 and 6 in the main text.

S. 3 Datafit of the *P*-wave signals diffracted along the solid–liquid boundary

Figure S3.1 shows the data fit for several differential travel times of core-sensitive seismic phases obtained from the joint inversion results. These include two seismic phases that traverse the core (SKS), recorded on sols 976 and 1000 (a sol corresponds to a Martian day, with sol 0 marking the InSight landing), and one seismic phase diffracted along the solid–liquid boundary of the core recorded on sol 1000. For non-BML models, this diffracted phase is interpreted as a P wave traveling along the core–mantle boundary, analogous to Earth's Pdiff. For BML models, however, this seismic wave is considered to diffract along the base of the mantle just above the BML, then propagate downward through the BML and reflect at the core–mantle boundary before returning to the surface (Samuel et al., 2023). While non-BML models provide a reasonable fit to the SKS arrival on sol 976 (Figure S3.1d–f), BML models, especially with EH45 and TA mantle compositions, show improved fits for SKS arrivals on both sols (Figure S3.1l–m). As previously shown by Samuel et al. (2019) using the EH45 mantle composition with a fixed Mg#, the fit to the P diffracted wave recorded on sol 1000 is significantly improved in BML models (Figure S3.1i–k) compared to non-BML models (Figure S3.1a–c).

S. 4 Distributions of epicentral distances

The output distributions of epicentral distances from the joint inversion are shown in Figure S4.1. The two peaks at 58.5 and 126.09 degrees correspond to the confirmed meteorite impacts S1094b and S1000a, whose locations were validated by orbital imaging (Kim et al., 2022; Posiolova et al., 2022). The highest concentration of events, around $\sim$30 degrees, corresponds to the Cerberus Fossae cluster (e.g., Drilleau et al., 2022). For non-BML models, epicentral distances show minimal variation across mantle compositions, differing by no more than 1 degree. In BML models, the differences between EH45 and TA remain under 1 degree, but can increase up to 3 degrees when the YM composition is considered. Between BML and non-BML models, the maximum difference in event locations is about 1.5 degrees for EH45 and TA compositions, and up to 3.5 degrees for YM.

S. 5 Attenuation structure and tidal dissipation

Our inversion output can be used to deduce shear attenuation, Q_μ, along the planet radius, r. Similar to viscosity, the attenuation $1/Q_\mu$ depends on temperature (T) and pressure (P), and is a function of frequency (ω) (Jackson et al., 2002; Efroimsky & Lainey, 2007; Smrekar et al., 2019; Samuel et al., 2019):

$$Q_\mu(r,\omega) \cong Q_0 \left[\omega \exp\left(\frac{E^* + P(r)V^*}{R\,T(r)}\right)\right]^{\alpha_q}, \tag{S5.1}$$

where R is the gas constant, and the power-law exponent α_q modulates the frequency dependence of the attenuation. Q_0 is a constant adjusted for each output model to match constraints on Mars' global degree-two shear attenuation, Q_2, at the frequency of the main Phobos tide (5 h 55 min): $Q_2 \cong 95 \pm 10$ (Bills et al., 2005; Khan et al., 2018; Pou et al., 2022). Q_2 is computed from Q_μ following the approach used in Samuel et al. (2019); Khan et al. (2004). Q_0 implicitly contains information on parameters determining the rheology of the mantle (*i.e.*, reference grain size and exponent or relaxation time scales). While more explicit models could be considered for $Q_\mu(r,\omega)$ (*e.g.*, Andrade, Burgers (Jackson & Faul, 2010; Renaud & Henning, 2018)) they would display dependencies on P, T and ω as Equation (S5.1) does (Smrekar et al., 2019; Pou et al., 2022; Guinard et al., 2025). All the parameters in Equation (S5.1) are known for each model, except for α_q. The latter was varied within bounds considered in the literature: $\alpha_q \simeq 0.1$ and 0.3 (Jackson & Faul, 2010; Khan et al., 2018; Smrekar et al., 2019; Pou et al., 2022; Samuel et al., 2023).

Figure S5.1 shows the resulting quality factor profiles in the solid silicate envelope, above a planetary radius higher than 1850 km. This corresponds to similar apparent core radii (*i.e.*, the radius of the metallic core plus the thickness of the molten BML, when present) at 1 Hz for the 100 non-BML and BML output models with the lowest misfit to the data, and for the three compositions considered. Because non-BML models are associated with hotter temperatures than BML models (Table 3), they exhibit higher seismic attenuation (lower Q_μ). This is further amplified by smaller frequency dependence of Q (lower α_q values). Consequently, non-BML models with low frequency dependence of attenuation (*i.e.*, $\alpha_q < 0.2$) systematically exhibit stronger seismic attenuation beyond minimum bounds recently inferred for Mars' solid mantle at seismic frequency (Li et al., 2025) (panels a,c,e in Figure S5.1), while BML models remain above this minimum bound (panels b,d,f in Figure S5.1).

S. 6 Influence of the thermodynamical database

Figures S6.1 and S6.2 show the data fit estimate for the joint inversion considering non-BML and BML models, using the thermodynamical database of Stixrude & Lithgow-Bertelloni (2011).

References

Bills, B. G., Neumann, G. A., Smith, D. E., & Zuber, M. T. (2005). Improved estimate of tidal dissipation within Mars from MOLA observations of the shadow of Phobos. *Journal of Geophysical Research*, *110*(E7), doi:10.1029/2004JE002376.

Civet, F., & Tarits, P. (2014, August). Electrical conductivity of the mantle of Mars from MGS magnetic observations. *Earth, Planets and Space*, *66*(1), 85. doi: 10.1186/1880-5981-66-85

Drilleau, M., Samuel, H., Garcia, R. F., Rivoldini, A., Perrin, C., Michaut, C., … Banerdt, W. B. (2022). Marsquake locations and 1-D seismic models for Mars from InSight data. *Journal of Geophysical Research: Planets*, *127*(9), e2021JE007067. doi: https://doi.org/10.1029/2021JE007067

Duncan, M. S., Schmerr, N. C., Bertka, C. M., & Fei, Y. (2018). Extending the solidus for a model iron-rich martian mantle composition to 25 gpa. *Geophysical Research Letters*, *45*(19), 10,211-10,220. doi: https://doi.org/10.1029/2018GL078182

Efroimsky, M., & Lainey, V. (2007). Physics of bodily tides in terrestrial planets and the appropriate scales of dynamical evolution. *Journal of Geophysical Research*, *112*(E12), E07004. (doi:10.1029/2007JE002908)

Guinard, A., Fienga, A., Mémin, A., & Ganino, C. (2025). Coupled tidal tomography and thermal constraints for probing Mars viscosity profile. *Icarus*, *425*(September 2024), 116318. Retrieved from `https://doi.org/10.1016/j.icarus.2024.116318` doi: 10.1016/j.icarus.2024.116318

Jackson, I., & Faul, U. H. (2010). Grainsize-sensitive viscoelastic relaxation in olivine: Towards a robust laboratory-based model for seismological application. *Physics of the Earth and Planetary Interiors*, *183*, 151-163. doi: 10.1016/j.pepi.2010.09.005

Jackson, I., Fitz Gerald, J. D., Faul, U. H., & Tan, B. H. (2002). Grainâsizeâsensitive seismic wave attenuation in polycrystalline olivine. *Journal of Geophysical Research: Solid Earth*, *107*(B12), 1–16. doi: 10.1029/2001jb001225

Khan, A., Liebske, C., Rozel, A., Rivoldini, A., Nimmo, F., Connolly, J. A. D., … Giardini, D. (2018). A Geophysical Perspective on the Bulk Composition of Mars. *Journal of Geophysical Research: Planets*, *224*(2-4), doi:10.1002/2017JE005371.

Khan, A., Mosegaard, K., Williams, J. G., & Lognonné, P. (2004, jan). Does the Moon possess a molten core? Probing the deep lunar interior using results from LLR and Lunar Prospector. *Journal of Geophysical Research E: Planets*, *109*(9), 80. doi: 10.1029/2004JE002294

Kim, D., Banerdt, W. B., Ceylan, S., Giardini, D., Lekić, V., Lognonné, P., … Panning, M. P. (2022). Surface waves and crustal structure on mars. *Science*, *378*(6618), 417-421. doi: 10.1126/science.abq7157

Konopliv, A. S., Park, R. S., Rivoldini, A., Baland, R. M., Le Maistre, S., Van Hoolst, T., … Dehant, V. (2020). Detection of the Chandler Wobble of Mars From Orbiting Spacecraft. *Geophysical Research Letters*, *47*(21), 1–9. doi: 10.1029/2020GL090568

Li, J., Hua, J., Ferrand, T. P., Pou, L., Huang, Q., Allibert, L., … Zhou, T. (2025). Evidence for weak seismic attenuation in Mars' deep mantle. *Communications Earth and Environment*, *6*(1), 1–11. doi: 10.1038/s43247-025-02664-9

Posiolova, L. V., Lognonné, P., Banerdt, W. B., Clinton, J., Collins, G. S., Kawamura, T., … Zenhäusern, G. (2022). Largest recent impact craters on mars: Orbital imaging and surface seismic co-investigation. *Science*, *378*(6618), 412-417. doi: 10.1126/science.abq7704

Pou, L., Nimmo, F., Rivoldini, A., Khan, A., Bagheri, A., Gray, T., … Giardini, D. (2022). Tidal Constraints on the Martian Interior. *Journal of Geophysical Research: Planets*, *127*(11). doi: 10.1029/2022JE007291

Renaud, J. P., & Henning, W. G. (2018). Increased Tidal Dissipation using Realistic Rheological Models: Implications for the Thermal History of Io and Tidally Active Extrasolar Planets. *The Astrophysical Journal*, *857*(2), 1–30.

Samuel, H., Drilleau, M., Rivoldini, A., Xu, Z., Huang, Q., Garcia, R. F., … Banerdt, W. B. (2023). Geophysical evidence for an enriched molten silicate layer above Mars's core. *Nature*, *622*, 712–717. (doi: 10.1038/s41586-023-06601-8)

Samuel, H., Lognonné, P. H., Panning, M., & Lainey, V. (2019). The rheology and thermal history of mars revealed by the orbital evolution of Phobos. , *569*, 523–527. (doi:10.1038/s41586-019-1202-7)

Smrekar, S. E., Lognonné, P., Spohn, T., Banerdt, B., Breuer, D., Christensen, U., … Wieczorek, M. (2019). Pre-mission insights on the interior of mars. *Space Science Reviews*, *215*, doi:10.1007/s11214-018-0563-9.

Stixrude, L., & Lithgow-Bertelloni, C. (2011). Thermodynamics of mantle minerals - II. Phase equilibria. *Geophysical Journal International*, *184*(3), 1180–1213. doi: 10.1111/j.1365-246X.2010.04890.x

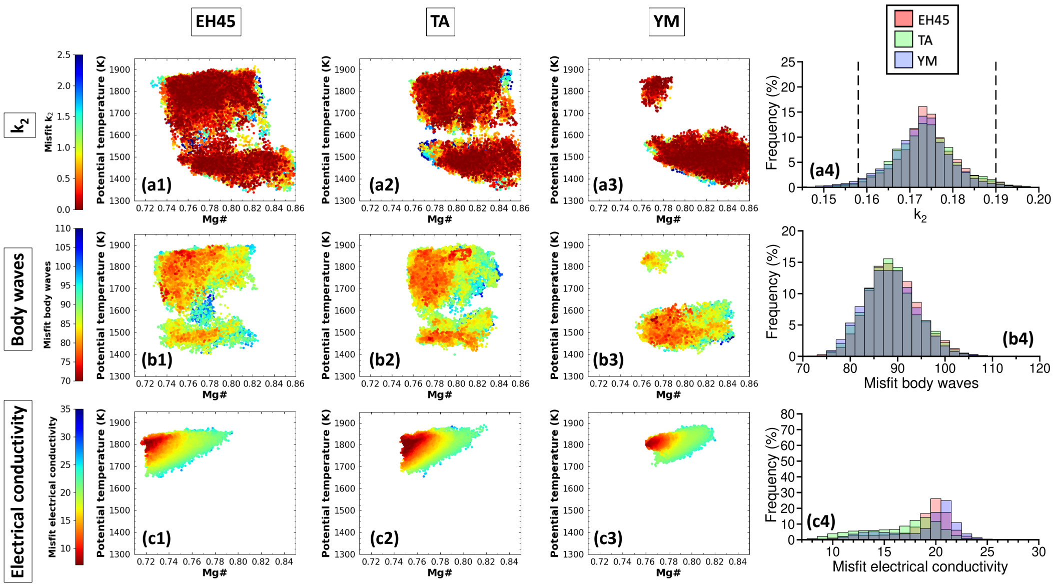

Figure S1.1. Data fit estimates of the individual inversion of the different data sets, for the non-BML set. The first three columns show T_p as a function of Mg# for the three compositions. In panels (a1-a3), (b1-b3), and (c1-c3), the color refers to the misfit value estimated for k_2, the body wave arrival times, the electrical conductivity, and all three data sets, respectively. Red and blue colours are small and large misfit values, respectively. (a4) shows the k_2 distribution. The black dashed lines show the 2σ uncertainty around the value of Konopliv et al. (2020) ($k_2 = 0.174 \pm 0.016$). Panels (b4, c4) display the misfit distributions of body wave arrival times and electrical conductivity, respectively. In panels (a4, b4, c4), the distributions considering EH45, TA, and YM compositions are displayed in red, green, and blue, respectively.

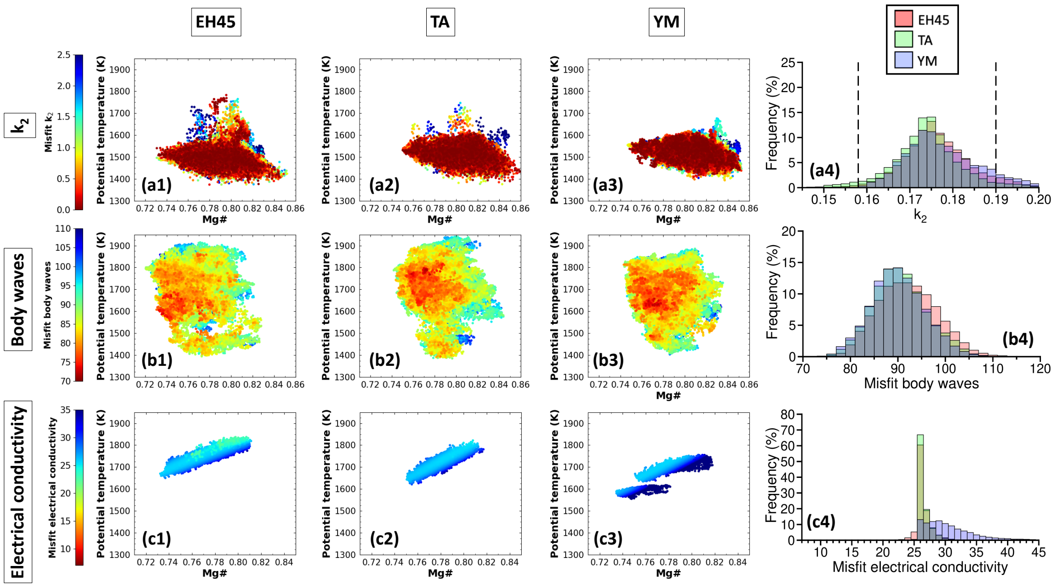

Figure S1.2. Data fit estimates of the individual inversion of the different data sets, for the BML set. The first three columns show T_p as a function of Mg# for the three compositions. In panels (a1-a3), (b1-b3), and (c1-c3), the color refers to the misfit value estimated for k_2, the body wave arrival times, the electrical conductivity, and all three data sets, respectively. Red and blue colours are small and large misfit values, respectively. (a4) shows the k_2 distribution. The black dashed lines show the 2σ uncertainty around the value of Konopliv et al. (2020) ($k_2 = 0.174 \pm 0.016$). Panels (b4, c4) display the misfit distributions of body wave arrival times and electrical conductivity, respectively. In panels (a4, b4, c4), the distributions considering EH45, TA, and YM compositions are displayed in red, green, and blue, respectively.

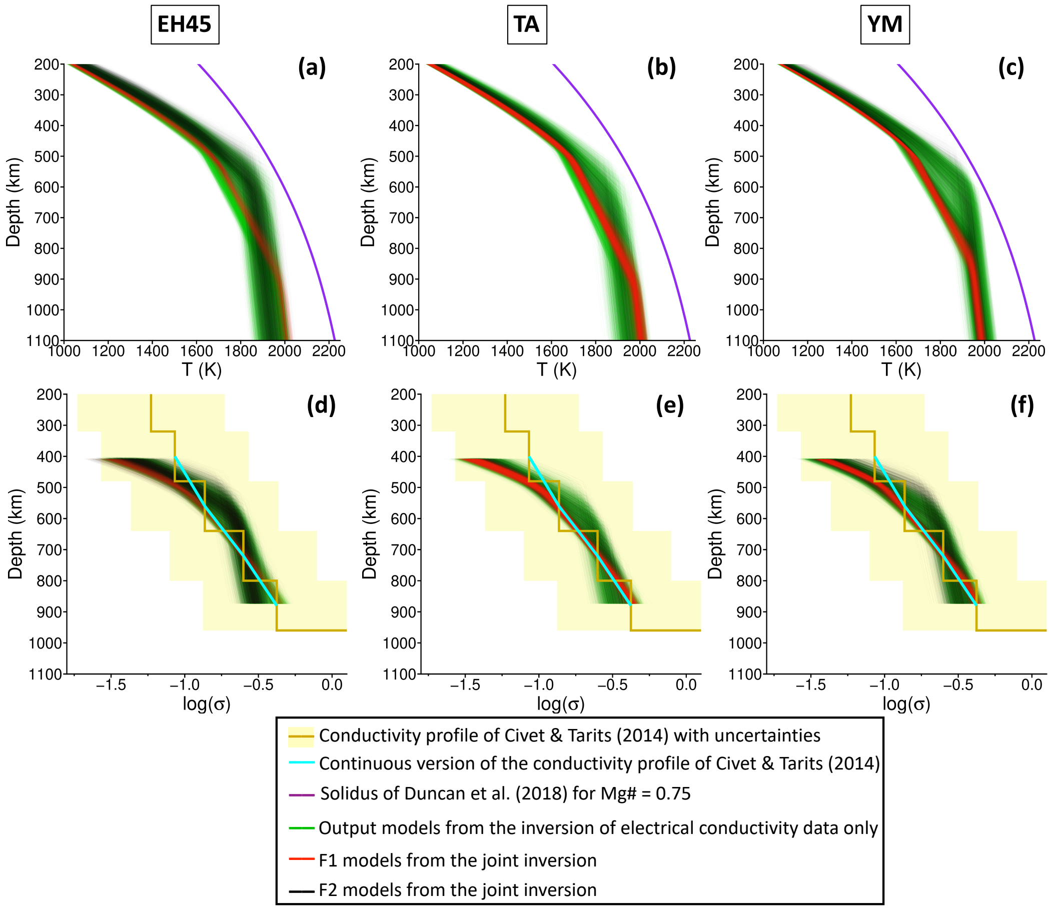

Figure S2.1. Temperature and electrical conductivity output profiles for the non-BML set. Panels (a, b, c) display the output temperature profiles, while panels (d, e, f) show the output electrical conductivity profiles for the three compositions. In panels (a, b, c), the solidus from Duncan et al. (2018) estimated for Mg#=0.75 is shown in purple. In panels (d, e, f), the electrical conductivity profile from Civet & Tarits (2014) is shown in khaki, with its uncertainties represented in yellow. The continuous version of the Civet & Tarits (2014) conductivity profile (see Section 2), to which the synthetic conductivity profiles are compared in the inversion, is depicted in cyan. The output profiles for families F1 and F2 (joint inversion) are represented in red and black, respectively. The output profiles of the inversion of electrical data only are shown in green. The output electrical conductivity profiles are shown only between 400 and 900 km depth, as this is the range over which they are compared with the continuous version of the conductivity profile from Civet & Tarits (2014).

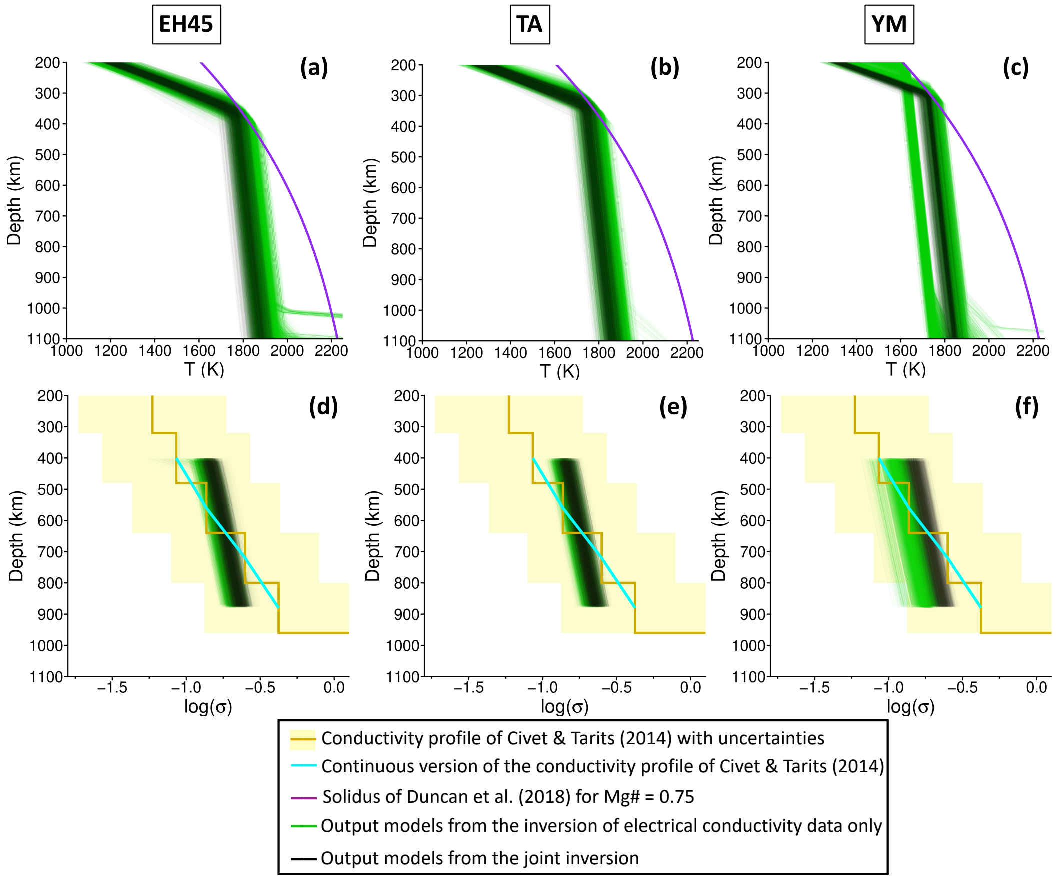

Figure S2.2. Temperature and electrical conductivity output profiles for the BML set. Panels (a, b, c) display the output temperature profiles, while panels (d, e, f) show the output electrical conductivity profiles for the three compositions. In panels (a, b, c), the solidus from Duncan et al. (2018) estimated for Mg#=0.75 is shown in purple. In panels (d, e, f), the electrical conductivity profile from Civet & Tarits (2014) is shown in khaki, with its uncertainties represented in yellow. The continuous version of the Civet & Tarits (2014) conductivity profile (see Section 2), to which the synthetic conductivity profiles are compared in the inversion, is depicted in cyan. The output profiles are represented in black. The output profiles of the inversion of electrical data only are shown in green. The output electrical conductivity profiles are shown only between 400 and 900 km depth, as this is the range over which they are compared with the continuous version of the conductivity profile from Civet & Tarits (2014).

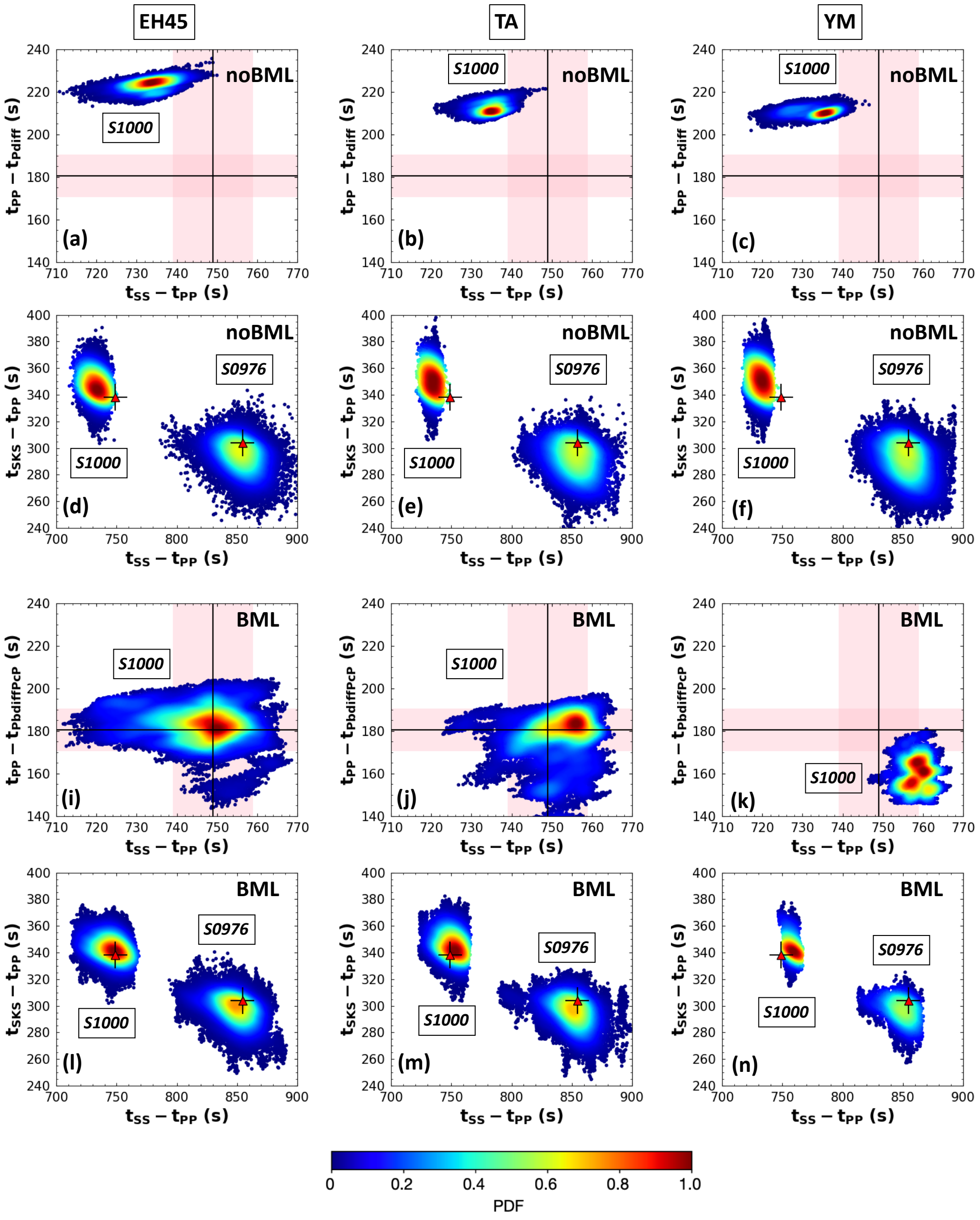

Figure S3.1. Data fit for the differential travel times recorded on sols 1000 and 976 of the InSight mission, comparing models without (a–f) and with (i–n) a BML. Results are presented as probability density functions (PDFs), with blue indicating low probability and red indicating high probability. The right, middle, and left columns correspond to the EH45, TA, and YM mantle compositions, respectively. For models without a BML, panels (a–c) show the differential travel times on sol 1000 between PP and Pdiff as a function of the differential travel time between SS and PP. The same analysis is shown for models including a BML in panels (i–j), where Pdiff is interpreted as PbdiffPcP. Observed differential times are indicated with black lines, and uncertainties are marked with pink bands. Panels (d–f) and (l–n) present differential times between SKS and PP versus the differential travel time between SS and PP for sols 1000 and 976. Observed arrival times and uncertainties are shown as markers with error bars.

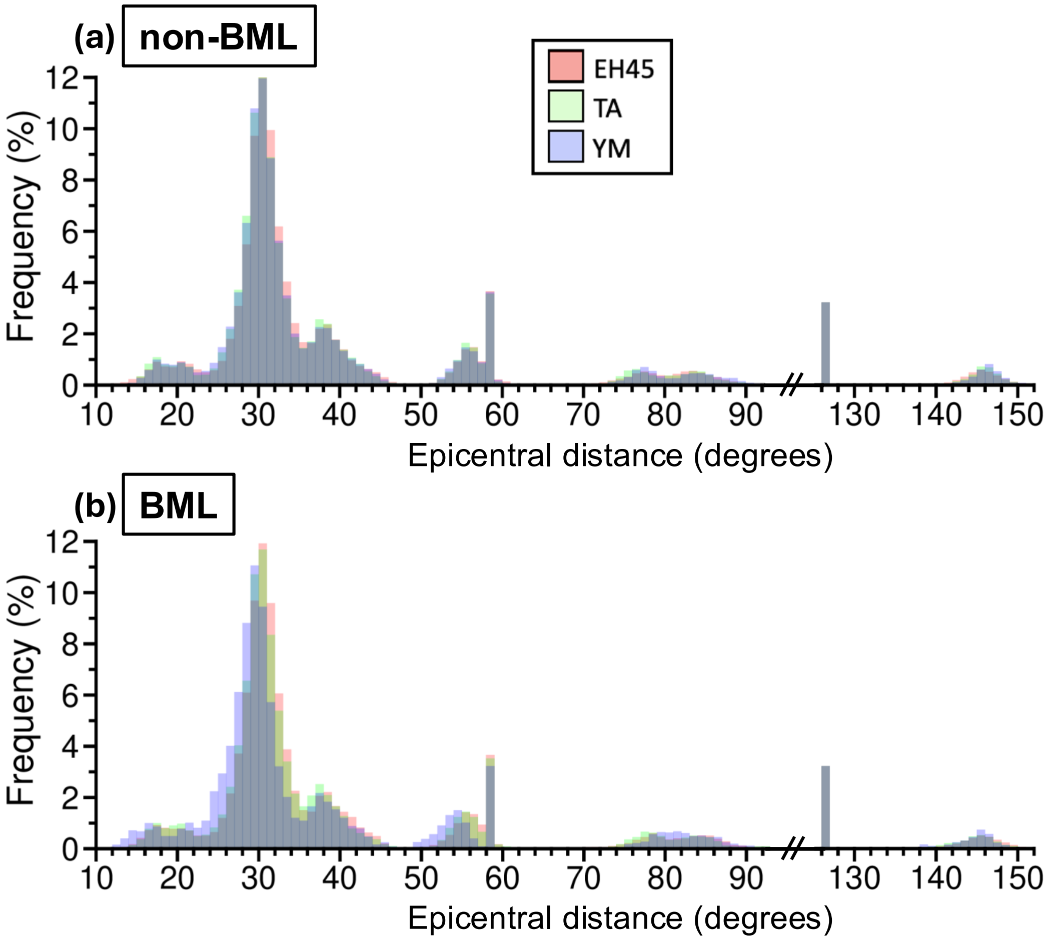

Figure S4.1. Output distributions of the epicentral distances of the 31 seismic events for (a) non-BML and (b) BML models. Distributions considering EH45, TA, and YM mantle compositions are shown in red, green, and blue, respectively.

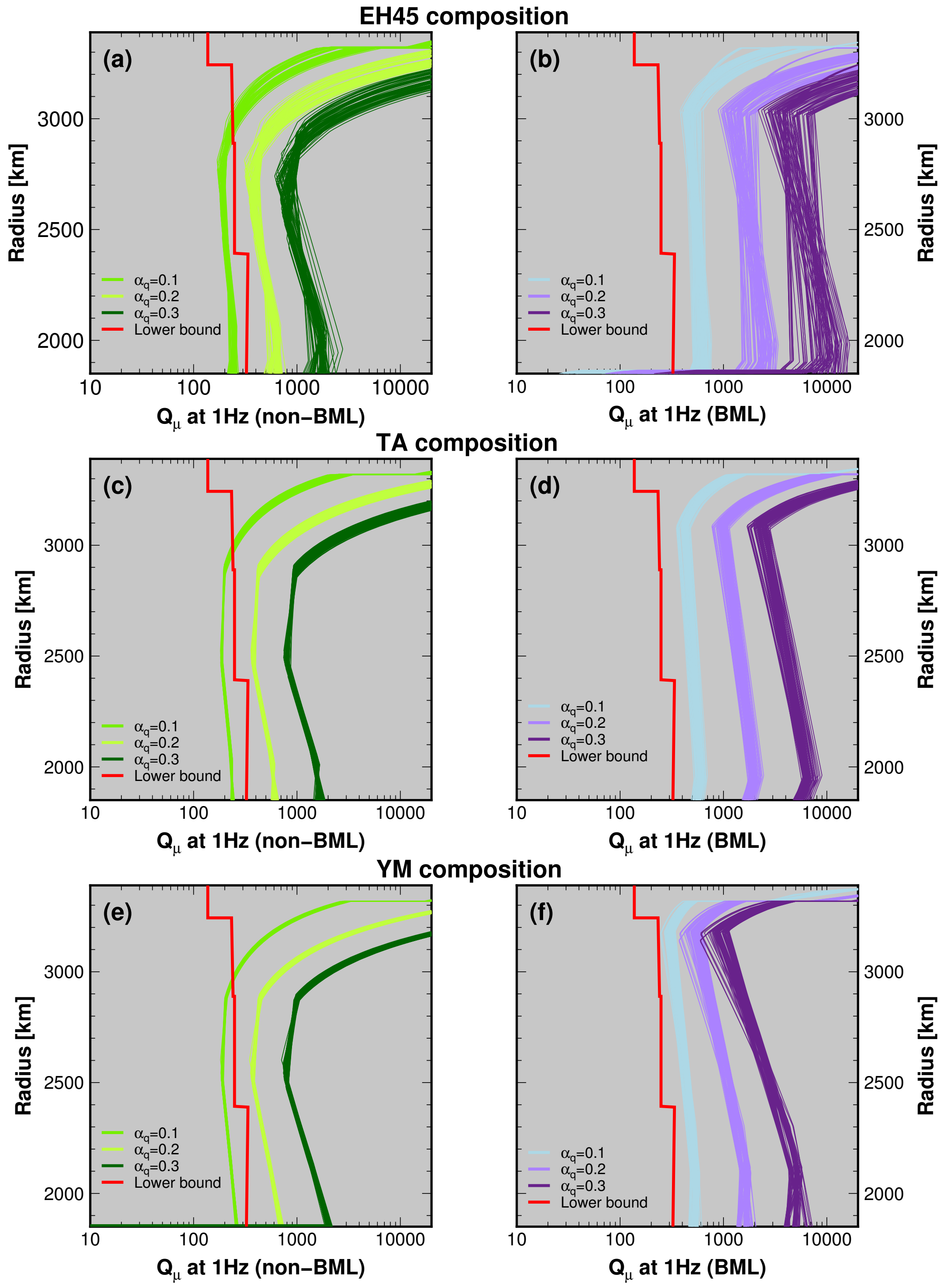

Figure S5.1. Attenuation at seismic frequency deduced from the 100 best non-BML and BML models, for the three compositions considered. Present-day shear quality profiles (Q_μ) at 1 Hz for the inversion set without a BML (left) and with a BML (right) for various frequency dependence (α_q) of the shear quality factor. The minimum bounds at seismic frequency derived from constraints on the P-wave quality factor, Q_P, in Li et al. (2025) are displayed in red, where we have assumed that $Q_\mu \cong (4/9)Q_P$. The obtained profiles match constraints on Mars' global degree-two shear attenuation, Q_2, at the frequency of the main Phobos tide: $Q_2 \cong 95 \pm 10$.

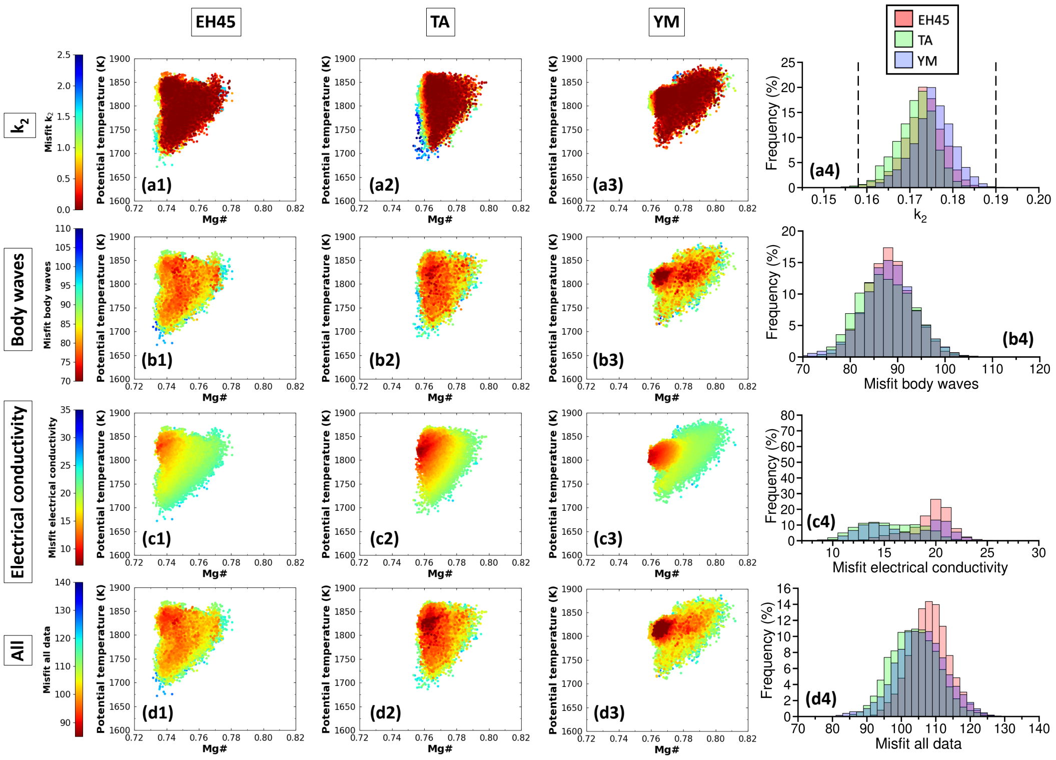

Figure S6.1. Data fit estimates of the joint inversion for the non-BML set, considering the thermodynamical database of Stixrude & Lithgow-Bertelloni (2011). The first three columns show T_p as a function of Mg# for the three compositions. In panels (a1-a3), (b1-b3), (c1-c3), and (d1-d3), the color refers to the misfit value estimated for k_2, the body wave arrival times, the electrical conductivity, and all three data sets, respectively. Red and blue colours are small and large misfit values, respectively. (a4) shows the k_2 distribution. The black dashed lines show the 2σ uncertainty around the value of Konopliv et al. (2020) ($k_2 = 0.174 \pm 0.016$). Panels (b4, c4) display the misfit distributions of body wave arrival times and electrical conductivity, respectively. (d4) shows the distribution of the total misfit value of the three data sets. In panels (a4, b4, c4, d4), the distributions considering EH45, TA, and YM compositions are displayed in red, green, and blue, respectively.

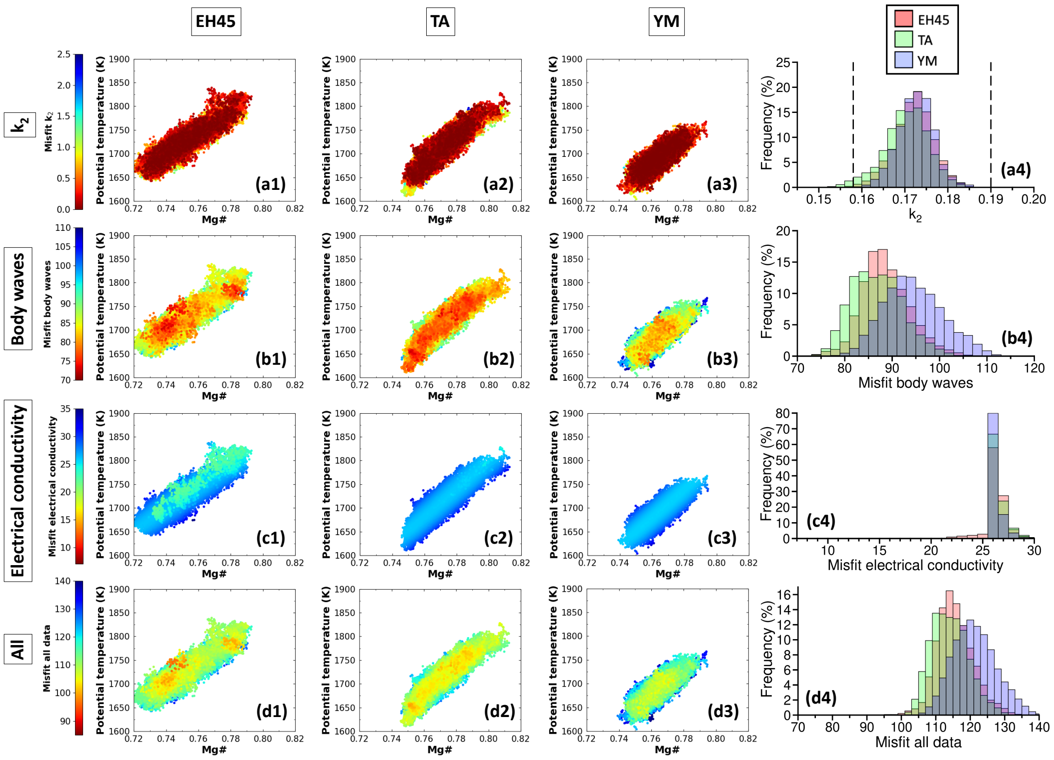

Figure S6.2. Data fit estimates of the joint inversion for the BML set, considering the thermodynamical database of Stixrude & Lithgow-Bertelloni (2011). The first three columns show T_p as a function of Mg# for the three compositions. In panels (a1-a3), (b1-b3), (c1-c3), and (d1-d3), the color refers to the misfit value estimated for k_2, the body wave arrival times, the electrical conductivity, and all three data sets, respectively. Red and blue colours are small and large misfit values, respectively. (a4) shows the k_2 distribution. The black dashed lines show the 2σ uncertainty around the value of Konopliv et al. (2020) ($k_2 = 0.174 \pm 0.016$). Panels (b4, c4) display the misfit distributions of body wave arrival times and electrical conductivity, respectively. (d4) shows the distribution of the total misfit value of the three data sets. In panels (a4, b4, c4, d4), the distributions considering EH45, TA, and YM compositions are displayed in red, green, and blue, respectively.